Journal of Marine Research, 63, 579–600, 2005

Effect of air-sea heat exchange on seasonal transport variation of the Kuroshio

by Toshihiro Sakamoto[1]

ABSTRACT

Observations up to the present indicate that the climatological volume transports of the Kuroshio have an annual range of at most 10 Sv and a maximum in summer, both of which are inconsistent with the nontopographic Sverdrup relation. We show that these observed properties may be reproduced using a two-layer planetary geostrophic model with variable bottom topography if we take into account sea-surface heat flux, as well as large interface displacements associated with layer outcropping. The thermal forcing is represented by seasonally changing the reduced gravity so that the available potential energy of the model ocean is decreased in winter and increased in summer, consistent with the seasonal air-sea heat exchange. From numerical experiments we find that the bottom topography accelerates conversion between available potential energy and kinetic energy of the barotropic flow so as to compensate for the change in the energy storage due to the heat transfer. In particular, winter cooling intensifies conversion from barotropic kinetic energy to available potential energy, leading to a further decrease in the winter transport, and the reverse takes place in summer, so that the summer transport may exceeds the winter transport.

1. Introduction

The available information is limited on the seasonal variations of volume transports of the Kuroshio because it is not easy to carry out high-density velocity measurements across the stream. Nevertheless, we can describe some collective features of the seasonal transport changes from observational efforts up to now, summarized in Table 1; see also Figure 1 for the locations of observations. Although not all the works cited are aimed mainly at the seasonal cycle and some results do not give definite transport values, we can compare the estimated transports in two major seasons. As in the case of the North Atlantic counterpart, both the annual mean transport and seasonal cycle of the Kuroshio seem to strongly depend on observation sites. For example, since it is known that the Kuroshio, after passing through the Tokara Strait, recirculates off Shikoku, Qiu (1992) and Isobe and Imawaki (2002) presented transport values by subtracting a contribution from the recirculating gyre. We also point out that direct current measurements in a shorter period tend to detect small-scale, high-frequency fluctuations (Ichikawa and Beardsley, 1993; Lee *et al.,* 2001).

1. Department of Earth and Planetary Science, Graduate School of Science, The University of Tokyo, Tokyo 113-0033, Japan. ***email: sakamoto@eps.s.u-tokyo.ac.jp***

Table 1. Observed seasonal cycle in the volume transport of the Kuroshio.

Reference	Year	Site	Method	Maximum transport (Sv) season	Minimum transport (Sv) season	Annual range (Sv)
Taft (1972)	1956–1964	135°10′E–138°40′E	referenced to 800 db	~54 summer	~42 spring	~12
Minami *et al.* (1978, 1979)	1956–1976	135°15′E	referenced to 1000 db	45 summer	38 winter	7
Blaha and Reed (1982)	1963–1974	Naze-Aburatsu	referenced to 1000 db	— summer	— —	10
Kawabe (1988)	1965–1983	Naze–Nishinoomote	sea level difference	— July	— Oct.	—
Qiu and Joyce (1992)*	1969–1988	137E	referenced to 1250 db	34.0†	32.1††	1.9
Ichikawa and Beardsley (1993)	1986–1988	East China Sea	referenced to surface	— summer	— —	10–20
Kagimoto and Yamagata (1997)	1973–1992	PN line	referenced to 700 db	~27 Aug.	~23 Nov.	~4
Ichikawa and Chaen (2000)	1981–1992	PN line	referenced to surface	32.14 summer	20.04 winter	12.1
Lee *et al.* (2001)	1989–1996	24N	sea level difference	~24 summer	~20 fall	~4
Lee *et al.* (2001)	1994–1996	East of Taiwan	moorings	~36 Sep.	~25 Mar.	~11
Isobe and Imawaki (2002)	1993–2001	ASUKA line	altimetry + ADCP	48 Sep.	35 Dec.	13
Zhang *et al.* (2002)	1989–1996	Ishigaki-Keelung	sea level difference	~24 July	~20 Oct.	~4

*See also Qiu (1992).
†July mean.
††January mean.

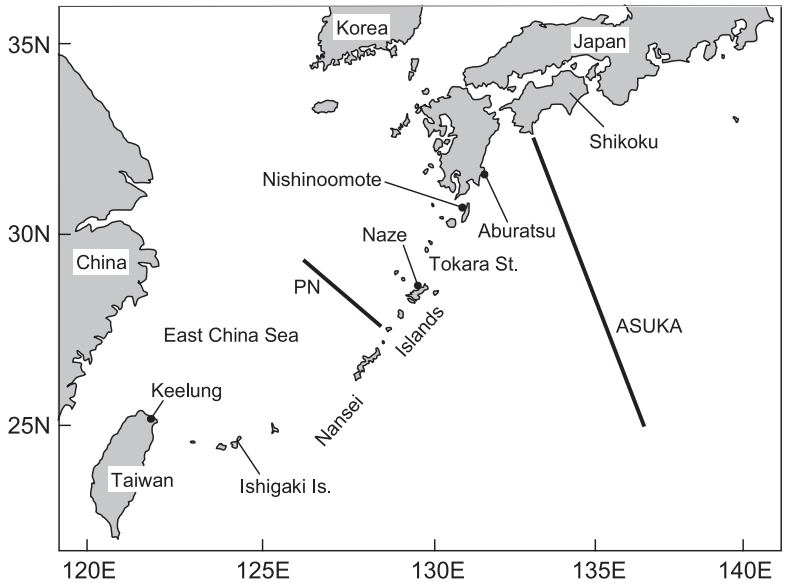

Figure 1. Map of the Kuroshio region off Japan, showing locations of observation sites which are referred to in Table 1.

Despite these difficulties, we can say with fair confidence that the annual range of the transport variation is around 10 Sv or less and that the summer transport is greater than the winter transport. Both properties are inconsistent with the annual cycle of the Sverdrup transport calculated using the wind data, first pointed out by Blaha and Reed (1982) after similar findings about the Florida Current (Niiler and Richardson, 1973; Schott *et al.,* 1988; Lee *et al.,* 2001). This implies that if we disregard such nonlinear processes as instabilities, the rotating solid earth must participate in regulating the barotropic behavior of the subtropical gyre including the Kuroshio.

Sakamoto and Yamagata (1996) proposed a basic mechanism that qualitatively solves the first discrepancy, the reduction of annual range. They employed the concept of JEBAR (Joint Effect of Baroclinicity and Bottom Relief) from a more liberated viewpoint in order to interpret results of their numerical experiments with a two-layer planetary geostrophic model. In winter, the water column with a large amount of negative vorticity put by the strong subtropical wind stress interacts vigorously with a sloping bottom to extract a positive angular momentum from the rotating solid earth, so that the column's negative vorticity is partly canceled. As a result, the subtropical gyre characterized by negative vorticity, and hence, its western boundary current is weakened. During this period, the decreased kinetic energy is stored in the form of available potential energy. This essentially barotropic process is closely analogous to mountain pressure torque in dynamic meteorology (Holton, 1992). In summer, even though the subtropical winds are very weak, the water column can still get negative vorticity by relaxing the baroclinic field over the

bottom slope to maintain the western boundary current. The available potential energy thus consumed during summer is, in turn, replenished in winter. The latter baroclinic processes, the heart of JEBAR, are needed in order to control not only the annual mean transport but also the amplitude of seasonal variations.

We have not yet explained the second discrepancy between the observations and the Sverdrup relation, the phase reversal of seasonal transport variations, by using such simple models. On the other hand, the result of a Kagimoto and Yamagata's (1997) simulation with a high-resolution ocean general circulation model appears to be in good quantitative as well as qualitative agreement with the observed climatology. This success encourages some OGCM modelers to claim that one needs to resolve fine structures of the bottom topography and/or eddy activities in order to reproduce a realistic seasonal cycle. However, regarding this particular problem, such elaborate calculations do not give immediate insight into pertinent mechanisms. Sakamoto and Yamagata's (1996) experimental results imply that we should improve the winter transport because it is still too large. It is thus natural to seek missing mechanisms that can reinforce the winter process mentioned above. Moreover, we expect that any changes in the winter transport may, in turn, affect the summer transport in a nontrivial manner.

The purpose of this study is to reproduce a realistic seasonal transport cycle using as simple a model as possible to identify definite mechanisms. We can accomplish this goal with the two-layer planetary geostrophic model used by Sakamoto and Yamagata (1996) with some modifications. The numerical model is presented in Section 2. Section 3 describes two sets of numerical experiments. In the first set of experiments we treat layer outcropping which may occur in such a model that the volume of the upper layer is conserved (Parsons, 1969; Huang, 1991; Sakamoto, 1999). We expect that large displacements of the thermocline associated with outcropping are more effective in "JEBAR rectification" (Sakamoto and Yamagata, 1996) than large topographic variations. In the second set of experiments we include the effects of air-sea heat exchange as a potential mechanism underlying the observed 180° out-of-phase relation. The results are presented in Section 4. Energy budget analysis, which was not carried out in the previous study, turns out to be helpful to unveil the role of bottom topography, especially in cases when time-dependent heat flux is taken into account. This is done in Section 5b after examining JEBAR from the point of view of vorticity in Section 5a.

2. The model

a. Basic equations and parameters

Our model ocean is a two-layer fluid contained in a rectangular β-plane basin bounded by vertical walls at $x = 0, L_e$ and $y = 0, L_n$, where x and y are the eastward and northward coordinates, respectively. The rigid lid approximation is made at the surface and the total depth of the ocean is $H(x, y)$.

We concentrate on motions whose lateral scale is so large that they are described by

Table 2. Values of parameters used in numerical experiments.

Parameter	Value	Parameter	Value
L_e	6000 km	L_n	2000 km
f_0	7.3×10^{-5} s^{-1}	β	2×10^{-11} m^{-1} s^{-1}
ρ_0	1000 kg m^{-3}	g'	0.02 m s^{-2}
R	2.4×10^{-4} m s^{-1}	K	1.6×10^{-3} m s^{-1}

planetary geostrophic dynamics in leading order approximation. The governing equations with forcing and damping terms are therefore

$$-fv_1 = -\frac{1}{\rho_0} p_x - \frac{R}{h_1}(u_1 - u_2) + \frac{\tau^x}{\rho_0 h_1}, \tag{1}$$

$$fu_1 = -\frac{1}{\rho_0} p_y - \frac{R}{h_1}(v_1 - v_2), \tag{2}$$

$$h_{1t} + (u_1 h_1)_x + (v_1 h_1)_y = 0, \tag{3}$$

$$-fv_2 = -\frac{1}{\rho_0} p_x + g' h_{1x} + \frac{R}{h_2}(u_1 - u_2) - \frac{K}{h_2} u_2, \tag{4}$$

$$fu_2 = -\frac{1}{\rho_0} p_y + g' h_{1y} + \frac{R}{h_2}(v_1 - v_2) - \frac{K}{h_2} v_2, \tag{5}$$

$$h_{2t} + (u_2 h_2)_x + (v_2 h_2)_y = 0. \tag{6}$$

Here, subscripts 1 and 2 refer to the upper and lower layers, respectively; (u_i, v_i) is the (eastward, northward) velocity; h_i is the layer thickness; p is the depth-independent pressure; $f = f_0 + \beta_0 y$ is the Coriolis parameter with β_0 constant; ρ_0 is a reference density; g' is the reduced gravity. The model ocean is driven by a wind stress that is assumed to have only a zonal component τ^x. The vertical transfer of momentum is parameterized by interfacial and bottom friction whose coefficients are R and K, respectively. Because of this simplification the boundary condition is no-normal flow at the lateral boundaries, namely,

$$\begin{aligned} u_i &= 0 \text{ at } x = 0, L_e, \\ v_i &= 0 \text{ at } y = 0, L_n. \end{aligned} \tag{7}$$

The parameterization is different from Rayleigh damping adopted by Sakamoto and Yamagata (1996). The main reason for this alteration is that the use of the interfacial friction will make it easier to treat layer outcropping in numerical calculations.

We prescribe the parameters typical of a subtropical gyre centered at 30N, as listed in Table 2. The upper layer thickness H_1 is varied in the numerical experiment. We have

confirmed in the vertical sections of σ_θ along 30.5N and 140.5E obtained from the Levitus climatology that σ_θ ranges from 24–25 around 100 m depth to 27.4 at 1200 m depth and increases more gradually at greater depths. Thus it seems reasonable to set $H_1 =$ 200–800 m with $g' = 0.02$ m s^{-2}. The friction coefficients are chosen arbitrarily, mainly restricted by grid resolution as usual.

The wind stress is assumed to depend only on y in space and in most calculations its time dependence is simplified such that

$$\tau^x = \tau_0\left(\cos\frac{2\pi t}{T} + 1\right)\sin\frac{\pi y}{L_n}, \tag{8}$$

where $\tau_0 = 0.1$ N m^{-2} and $T = 86400 \times 360$ sec, corresponding to 1 model year which contains 360 days ($t = 0$ is set as January 1). The amplitude thus changes between 0 on July 1 and 0.2 N m^{-2} on January 1 at $y = 0$ and L_n. An alternative form as a function of t will be given later. We prescribe the bottom topography of the form

$$H = H_0 - H_s\exp\left[-\frac{x^2}{l^2}\right] - H_r\exp\left[-\frac{(x - x_r)^2}{l^2}\right], \tag{9}$$

which is composed of a western continental slope whose height is H_s and a meridional ridge whose height is H_r and whose axis is located at $x = x_r$. In this expression, both topographic features have a common characteristic half width l for simplicity. We set $H_0 = 4000$ m, $l =$ 400 km and $x_r = 1000$ km to imitate the bathymetry south of Japan including the Izu-Ogasawara Ridge, whereas H_s and H_r are varied in numerical experiments.

b. Numerical procedure

For numerical calculations the basic equations are finite-differenced and the discretized variables are arranged on a regularly spaced, staggered B-grid (e.g. Haltiner and Williams, 1980) with a spacing of 40 km. Layer outcropping and associated large gradients of the interface may be numerically reproduced without spurious oscillations by using specially designed high-resolution schemes (e.g. Bogue *et al.,* 1986; Chassignet and Bleck, 1993; Cloke and Cullen, 1994; Salmon, 2002). Here we apply the explicit symmetric TVD scheme (Yee, 1987) to the flux terms in the continuity equation (3); the utility of this conservative scheme and several other TVD variants (e.g. Toro, 1997) has already been demonstrated by Sakamoto (2003). The resulting ordinary differential equation with respect to t is numerically integrated by using the second-order, two-stage Runge-Kutta method from the initial condition $h_1 = H_1$, $u_i = v_i = 0$ at all grid points. The pressure gradient terms in the momentum equations (1), (2), (4) and (5) are determined via the barotropic streamfunction ψ defined by

$$\boldsymbol{k} \times \nabla\psi = \boldsymbol{V}, \tag{10}$$

where $\boldsymbol{k}$ is the vertical unit vector and $\boldsymbol{V} = h_1\boldsymbol{v}_1 + h_2\boldsymbol{v}_2$ is the depth-integrated velocity. On the other hand, ψ is solved by using the SOR method under the boundary condition $\psi = 0$. Given

Table 3. Cases of numerical experiments.

Exp. no.	Fig. no.	H_1 (m)	H_s (m)	H_r (m)	Δ_g (m s^{-2})	θ (days)
A1	2, 3b, 5a, 6a, 7a, 8	200	3400	2000	—	—
A2	3a, 4a	200	2000	2000	—	—
A3	3a	300	2000	2000	—	—
A4	3a, 5b, 9	400	2000	2000	—	—
A5	3a	800	2000	2000	—	—
A6*	3b	200	3400	2000	—	—
A7	4a	200	1000	2000	—	—
A8	4a	200	3000	2000	—	—
A9	4b	200	2000	1000	—	—
A10	4b	200	2000	3000	—	—
F1†	3a, 4, 5, 8	200	0	0	—	—
F2*†	3b	200	0	0	—	—
F3†	9	400	0	0	—	—
B1	5a, 6b, 7b, 8	200	3400	2000	0.01	0
B2	5b, 9	400	2000	2000	0.004	60

*Wind forcing with weak summer maximum is applied; see (11).
†Calculation with flat bottom.

advanced quantities h_1 and ψ at all grid points, the velocity components are diagnosed. The maximal value of the time step Δt is found to become smaller as H_1 is increased; we set, for example, $\Delta t = 40$ min for $H_1 = 800$ m and 60 min for $H_1 = 200$ m. We have confirmed that the spin-up time required to establish a periodic state tends to be longer for smaller H_1, which is consistent with the expectation from the phase speeds of baroclinic long Rossby waves as mentioned above. At any rate, 15-year integration is found to be sufficient for almost all cases in the present experiments to assure that transient signals disappear.

3. The experiments

Two sets of numerical experiments are conducted as listed in Table 3. In Exp. A, we examine the effects of small values of H_1, the mean thickness of the upper layer, and in Exp. B, we examine the effects of varying g' as a function of time. The reason for this choice is that the conditions in both experiments are expected to contribute toward decreasing phase speeds of baroclinic long Rossby waves. In such situations the baroclinic adjustment becomes much less important on the annual time scale, which may help to intensify transfers of angular momentum from the solid earth to the barotropic water column through a sloping sea floor as mentioned before.[2]

Exp. A is divided into several cases. First, as a basic run, calculation is made with the

2. As an extreme case we may envisage a homogeneous ocean in which barotropic flows coming from the broad interior are perfectly blocked by a high meridional ridge and a steep continental slope, leaving little to the western boundary current.

smallest H_1 and the largest H_s throughout the present experiments (Exp. A1). We next examine the dependence of the seasonal transport cycle on H_1 (Exps. A2–A5). Then in Exp. 6 we compare the basic run with the case when the wind forcing is replaced by

$$\tau^x = \tau_0 \sin \frac{\pi y}{L_n} \times \max \left(\cos \frac{2\pi t}{T} + 1, \frac{1}{2} \cos \frac{4\pi t}{T} \right) \tag{11}$$

which has a weak maximum in July. Such a secondary peak is actually seen in the Sverdrup transport calculated using the observed wind data (Hellerman and Rosenstein, 1983); see Figure 1 of Sakamoto and Yamagata (1996). Finally, we change either H_s or H_r to investigate the relative importance between the density structure and topographic heights in determining the seasonal transport cycle (Exps. A7–A10). To give nontopographic transports for comparison we also carry out calculations with flat bottom as Exps. F1, F2 and F3, corresponding to Exps. A1, A6 and A4, respectively.

In Exp. B, on the other hand, we include a time variation of the density difference between the two layers. Here, we attribute this to heat exchange between the atmosphere and the upper layer of the model ocean, assuming that the surface mixed layer and the seasonal thermocline are embedded in the upper layer as usual. To see this explicitly we derive the potential energy equation from (3). The result is

$$\Phi_t + \nabla \cdot (2\Phi \boldsymbol{v}_1) = \boldsymbol{v}_1 \cdot \nabla\Phi + \tfrac{1}{2}\rho_0 h_1^2 g'_t, \tag{12}$$

where

$$\Phi = \tfrac{1}{2}\rho_0 g' h_1^2 \tag{13}$$

is the available potential energy. The source term in (12), which appears due to the nonzero time derivative of g', plays a role such that increasing (decreasing) g' corresponds to a positive (negative) heat transfer into the ocean. Therefore, by suitably choosing the functional form $g'(t)$, we may include the effects of winter cooling and summer heating without introducing any additional complexity into the present model. For further simplicity, we assume g' to oscillate sinusoidally with an annual period such that

$$g'(t) = g'_0 - \frac{\Delta_g}{2}\left[1 + \cos\left(\frac{2\pi t}{T} - \theta\right)\right], \tag{14}$$

where g'_0 is a constant which is fixed at the same value as g' in Table 2, Δ_g is an amplitude and θ denotes a phase delay. We demonstrate the following two cases. In Exp. B1 we treat a rather exaggerated case in which $\Delta_g = 0.01$ m s^{-2} and $\theta = 0$ in (14) so that the density difference between both layers becomes maximum in July due to heat gain in the first half of the year and minimum in January due to heat loss in the second half of the year. The values of H_1, H_s and H_r are the same as in Exp. A1. In Exp. B2 we choose $\Delta_g = 0.004$ m s^{-2} and $\theta = 60$ days, and the remainder is the same as in Exp. A4. In this case, heat loss attains its maximum in December.

The generation of barotropic flow by thermal effects is partly motivated by Stommel and Veronis (1980) who gave a theory of a steady barotropic flow in response to localized cooling in a two-layer fluid. This cooling was represented by conversion from light to dense water which mimics the formation of the 18°C water south of the Gulf Stream. Since we are concerned with the effects of seasonality in heat transfer, we assume here that g' is spatially uniform and that no diapycnal mixing is permitted.

4. Results

To see typical overall patterns of barotropic and baroclinic fields, Figure 2 shows a numerical solution for Exp. A1, drawn at 3-month intervals. For this value of H_1 (200 m) outcropping occurs in the north throughout the year and in the southeast in winter and spring; the figure demonstrates that the TVD scheme captures these outcropping lines without numerical instability. In the maps of h_1 we see that the depth of the interface reaches about 450 m in the west, forming a subtropical bowl. The horizontal pattern of the interface resembles that of the observed 26 σ_θ surface in the North Pacific calculated using the Levitus climatology. In the map of ψ we see that the gyre is split by the ridge, so that the streamfunction exhibits more than one maximum in all seasons. Since we are concerned with the transport of the Kuroshio, in particular, along the Nansei Islands, the term "transport" hereafter denotes the volume transport of the western boundary current for definiteness. We note that even without relative vorticity a recirculation may be produced near the western boundary owing to the interfacial and bottom friction (Welander, 1966), although we have confirmed that such a phenomenon becomes unimportant when the continental slope is sufficiently steep.

Figure 3a shows the annual transport cycle for Exps. A2–A5, together with Exp. F1 giving the Sverdrup transport. We note that an outcrop region appears when $H_1 = 300$ m or less and does not appear when $H_1 = 400$ m or larger. We see immediately that as H_1 is decreased up to 300 m the transport is reduced selectively in winter while there is little change in summer. The annual range is 5.4 Sv when $H_1 = 300$ m, only 6% of that of the Sverdrup transport. However, the annual range is not reduced further when outcropping occurs; the seasonal cycle when $H_1 = 200$ m closely resembles that when $H_1 = 300$ m except for a smaller annual mean transport in the former case.

Figure 3b compares the result for Exp. A1 and that for Exp. A6. We confirm that the transport associated with the wind forcing (11) is slightly larger throughout the year than that obtained with the standard wind forcing (8). However, the phase relation is unchanged, implying that the summer maximum of the wind strength is not a primary cause of the maximum transport in summer but increases the annual mean transport by increasing the net annual input of negative vorticity.

Figure 4 shows the results for various values of H_s and H_r (Exps. A2, A7–A10). We see that the annual range is reduced with increasing H_s (Fig. 4a), whereas the seasonal cycle is almost independent of H_r (Fig. 4b), indicating that the overall seasonal cycle is determined by a western continental slope of sufficient height. Comparing Figures 3 and 4, we find that

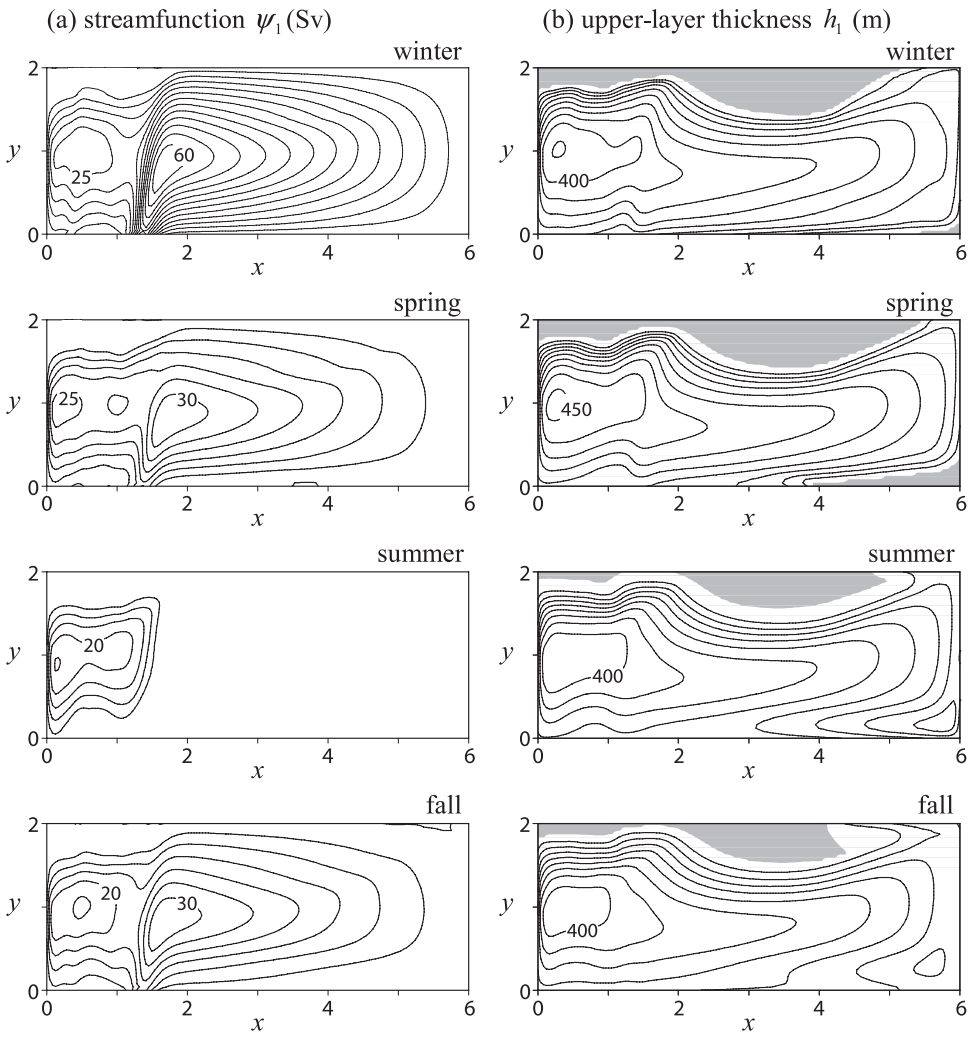

Figure 2. Contour lines of (a) barotropic streamfunction and (b) upper-layer thickness when (H_1, H_s, H_r) = (200, 3400, 2000 m) (Exp. A1). The maps are drawn every 3 months beginning with January 1. Contour intervals are 5 Sv in (a) and 50 m in (b). Outcropping regions are shaded in (b). Both the abscissa and the ordinate are scaled by 1000 km.

the annual range is more sensitive to the interface displacement than to the bottom topography.

The results of Exp. B are shown in Figure 5. Figure 5a compares the transport variation for Exp. B1 with that for Exp. A1. We see that the winter transport is further decreased as expected and, rather surprisingly, that the summer transport is increased compared with the case when $g' \equiv g'_0$. As a result, the seasonal cycle is about 180° out of phase with that of

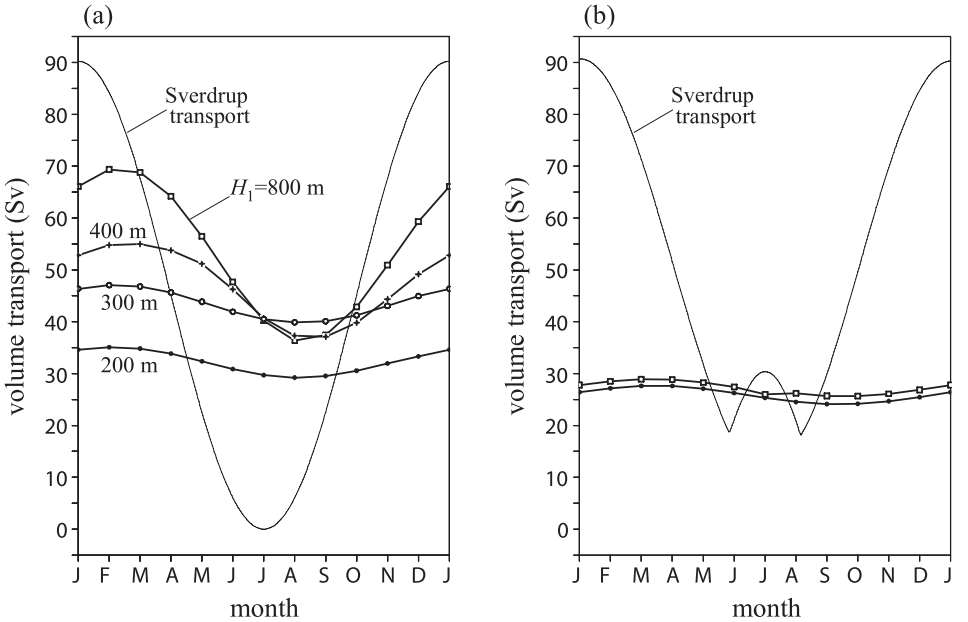

Figure 3. Barotropic transport of the western boundary current for (a) Exps. A2–A5, showing the dependence on the mean upper-layer thickness and (b) Exp. A6 (open squares), showing the effect of the wind forcing with a weak summer maximum inferred from the Sverdrup transport (thin solid line). In (b) the result for Exp. A1 is plotted with dots for comparison.

the Sverdrup transport. Figure 5b shows the case for Exp. B2 together with that for Exp. A4 for comparison. The seasonal cycle is greatly changed by the thermal forcing but this change is not a simple translation; the transport gradually increases from spring to summer and drops relatively rapidly in fall, which is in good qualitative agreement with some observed results in Table 1 (Kawabe, 1988; Kagimoto and Yamagata, 1997; Zhang *et al.,* 2002).

5. Discussion

As anticipated in Section 3 and demonstrated numerically in Section 4, decreasing H_1 and/or g' is compatible to a further reduction of the winter transport, although it is not easy to explain the reason why the transport is increased in summer when g' is varied seasonally. In this section we discuss the numerical results, first by resorting alternately to bottom pressure torque and JEBAR, and secondly based on global energy balance to address this question.

a. Vorticity dynamics

There are different ways to represent the vorticity balance (e.g. Mertz and Wright, 1992). If we put emphasis on the external aspect of bottom topography, we obtain the vorticity equation of the form

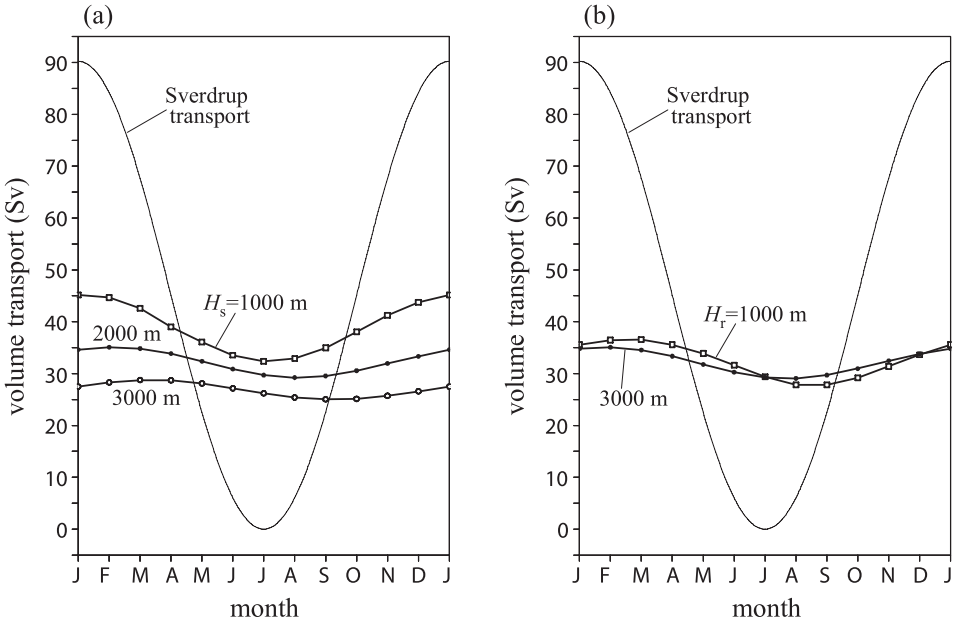

Figure 4. The same as Figure 3a but for (a) Exps. A2, A7, and A8, showing the dependence on the height of the western continental slope and (b) Exps. A9 and A10, showing the dependence on the height of the meridional ridge.

$$J(\psi, f) = \frac{1}{\rho_0} J(p_b, H) - \frac{1}{\rho_0} \tau_y^x - K(v_{2x} - u_{2y}), \tag{15}$$

where J denotes the Jacobian and p_b is the pressure at the bottom. In this formula, topographic effects are expressed by the first term on the right-hand side, called bottom pressure torque; when it is positive the water column extracts a positive angular momentum from the rotating solid earth. If this term is zero everywhere, (15) reduces to a nontopographic Sverdrup balance. Figure 6 shows distributions of the bottom pressure torque for Exps. A1 and B1 (cf. Fig. 5a). In winter, with and without seasonal heat fluxes, the bottom pressure torque is strongly positive on the eastern side of the ridge and weakly positive above the continental slope. This distribution reflects the basin-integrated values which are also shown in Figure 6. We thus confirm that in winter the subtropical gyre loses negative vorticity over the bottom slopes. In summer, the signs of the bottom pressure torque are reversed except near the western boundary but its magnitude appears to be much smaller than that in winter. The latter property verifies the relative importance of baroclinic processes in summer. We compare Figures 6a and 6b to find that the seasonal heat flux strengthens both the net positive pressure torque in winter and the net negative pressure torque in summer.

If, on the other hand, we make explicit the topographic beta effect, we obtain an alternative form of the vorticity equation

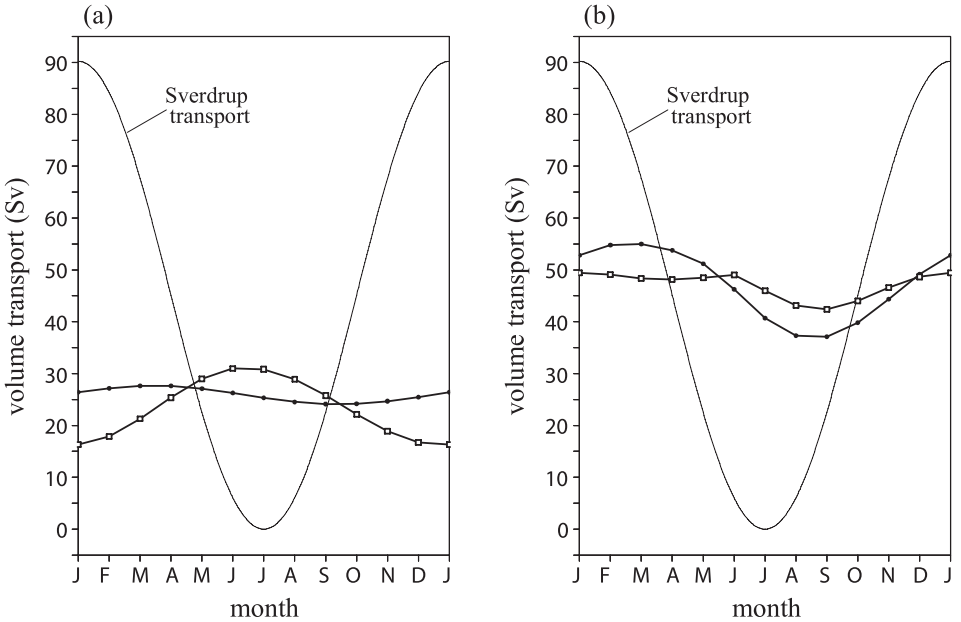

Figure 5. The same as Figure 3a but for (a) Exp. B1 (open squares) and (b) Exp. B2 (open squares), showing the effect of seasonal heat fluxes. The seasonal cycles for Exp. A1 and Exp. A4 are plotted with dots in (a) and (b), respectively.

$$J\left(\psi, \frac{f}{H}\right) = J\left(\frac{1}{2}\, g' h_1^2, \frac{1}{H}\right) - \frac{1}{\rho_0}\left(\frac{\tau^x}{H}\right)_y - K\left[\left(\frac{v_2}{H}\right)_x - \left(\frac{u_2}{H}\right)_y\right]. \tag{16}$$

Here, we consider a distorted β-plane whose "latitude circles" are the f/H contours and on this plane the forcing and dissipation terms are correspondingly altered. In this formula, bottom topography is linked with internal processes, appearing as the first term on the right-hand side, called the JEBAR term. If this term is zero everywhere, (16) reduces to a vorticity balance in a homogeneous ocean with variable bottom topography. Figure 7 shows distributions of the JEBAR term corresponding to Figure 6. We find that the basin-integrated contribution is always negative, so that JEBAR has a basin-wide tendency to drive a clockwise barotropic circulation throughout the year except possibly in regions where meridional gradients of the f/H contours are reversed. With and without seasonal heat fluxes, the total amount of negative vorticity produced by JEBAR is greater in summer than in winter, indicating again that baroclinic processes are more important in summer than in winter. Unlike the bottom pressure torque, the JEBAR term is dominant over the continental slope as though JEBAR plays a role of virtual forcing in driving the western boundary current over the continental slope. In fact, a typical strength of the JEBAR term is estimated to be $\sim 10^{-11}$ s^{-2} (cf. Fig. 7), whereas a typical strength of the wind forcing term in (16) is estimated to be $2\pi\tau_0/[\rho_0(H - H_s)L_n] \sim 5 \times 10^{-13}$ s^{-2} which is two orders of

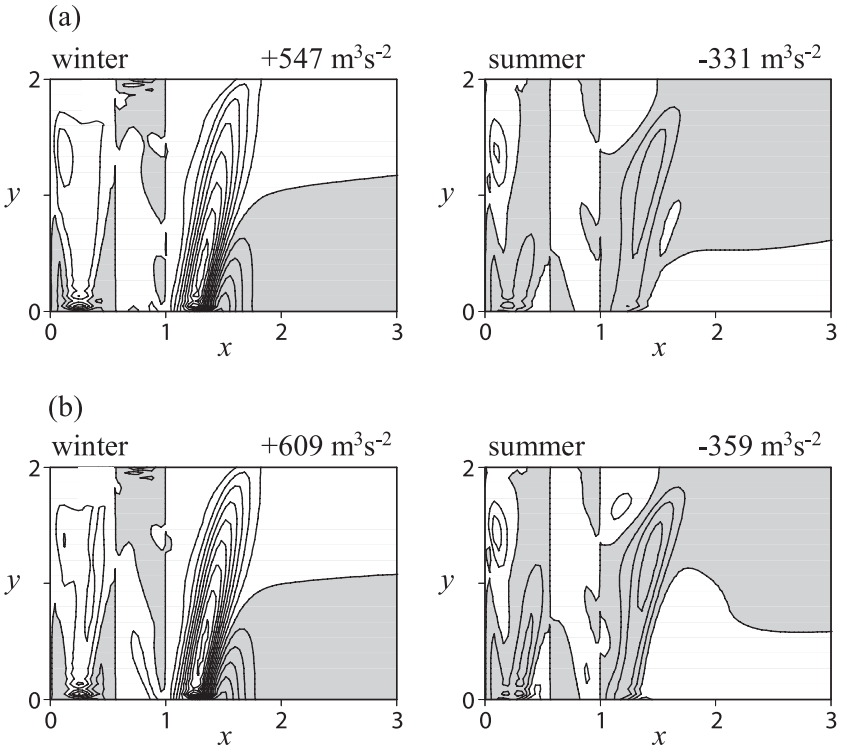

Figure 6. Distributions of bottom pressure torque for (a) Exp. A1 and (b) Exp. B1. Contour interval is 5×10^{-10} m s^{-2}. Regions of negative values are shaded. The numerical value attached to each panel is the basin integration in units of m^3 s^{-2}. Both the abscissa and the ordinate are scaled by 1000 km.

magnitude smaller than the JEBAR term. If we regard the JEBAR term as a driving agency, we may explain the results of Figures 3 and 4 as follows. The JEBAR term depends on the interface displacement in the form of ∇h_1^2, whereas it depends on the bottom slope merely in the form of ∇H^{-1}. On the other hand, the interface displacement increases as H_1 is decreased until outcropping occurs provided that the volume of the upper layer is conserved.

Comparing Figures 7a and 7b, we find that when the seasonal heat flux is included, the JEBAR-induced vorticity becomes weaker in winter and stronger in summer, in accord with the transport variation in Figure 5a. Since the JEBAR term is proportional to g', we are tempted to conclude that the seasonal cycle in Figure 5a is simply in phase with the prescribed seasonal cycle of g'. However, the latter viewpoint cannot explain the excess summer transport even if $g' \leq g'_0$ throughout the year. We should notice that the summer transport is affected by the preceding seasons as follows. Since g' is smaller than g'_0 in winter and spring, the Ekman pumping during these seasons deepens the subtropical bowl

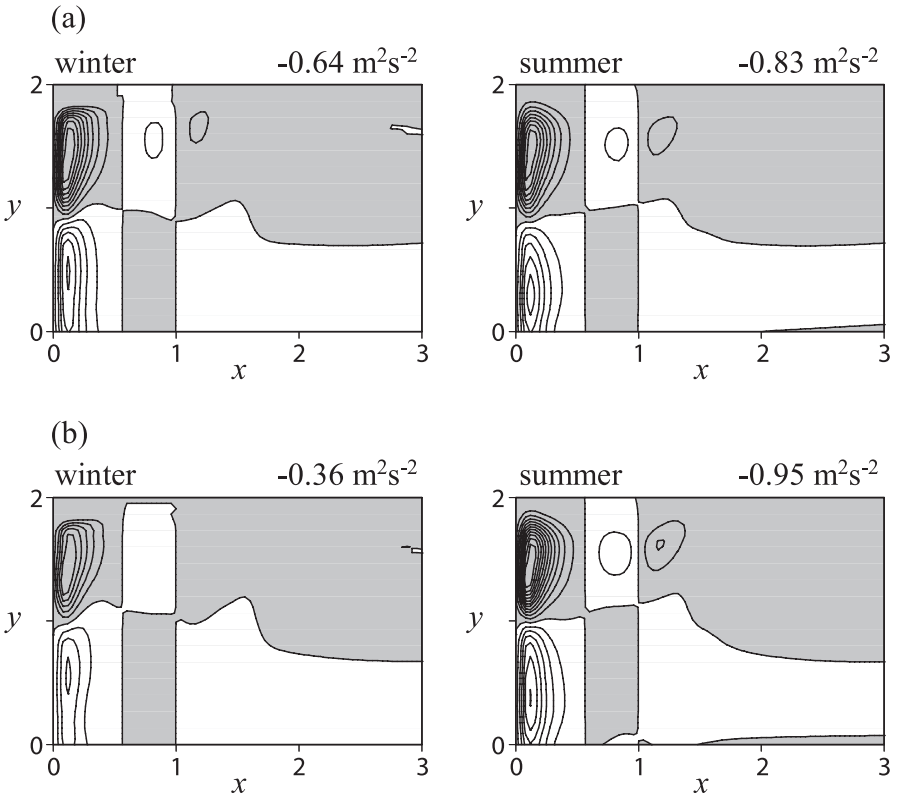

Figure 7. Distributions of values of the JEBAR term corresponding to Figure 6. Contour interval is 2×10^{-12} s^{-2}. Regions of negative values are shaded. The numerical value attached to each panel is the basin integration in units of m^2 s^{-2}. Both the abscissa and the ordinate are scaled by 1000 km.

more than in the case when $g' = g'_0$. Displacements of the interface remain larger in the succeeding summer due to the incompleteness of the baroclinic adjustment.

b. Energetics

From (1)–(5) we obtain the energy equations in the usual form

$$0 = W_p + \{\Phi, K\} + \tau^x u_1 + D \tag{17}$$

$$\Phi_t + \nabla \cdot (2\Phi \boldsymbol{v}_1) = -\{\Phi, K\} + Q. \tag{18}$$

The latter equation is a rewriting of (12) with the available potential energy (13). In these equations,

$$K = \sum_{i=1}^{2} \frac{1}{2} \rho_0 |\boldsymbol{v}_i|^2 h_i \tag{19}$$

is the total kinetic energy,

$$W_\mathrm{p} = -\boldsymbol{V} \cdot \nabla p_2 = -\nabla \cdot (p_2 \boldsymbol{V}) \tag{20}$$

is the work done by the pressure gradient force in the lower layer, $-\nabla p_2$,

$$\{\Phi, K\} = -\rho_0 g' h_1 \boldsymbol{v}_1 \cdot \nabla h_1 = -\boldsymbol{v}_1 \cdot \nabla \Phi, \tag{21}$$

denotes the rate of conversion from Φ to K,

$$D = -R\rho_0 |\boldsymbol{v}_1 - \boldsymbol{v}_2|^2 - K\rho_0 |\boldsymbol{v}_2|^2 \tag{22}$$

is dissipation, and

$$Q = \tfrac{1}{2} \rho_0 h_1^2 g'_t \tag{23}$$

corresponds to the heat flux as explained before. When we average (17) and (18) over the basin (denoted by angle brackets) and use the boundary condition (7), we obtain the basin-scale energy balance

$$0 = \langle \Phi, K \rangle + \langle \tau^x u_1 \rangle + \langle D \rangle, \tag{24}$$

$$\langle \Phi_t \rangle = -\langle \Phi, K \rangle + \langle Q \rangle, \tag{25}$$

where inner brackets have been removed for brevity. Obviously, the conversion term becomes a major source of kinetic energy when winds are weak, but $\langle \Phi, K \rangle$ does not necessarily produce a barotropic flow that is of primary concern. To avoid this ambiguity we rewrite (17) so that the barotropic flow $\boldsymbol{V}$ enters the conversion term. An appropriate form is

$$0 = W_\mathrm{p} + \{\Phi, K_\mathrm{bt}\} + \frac{\tau^x}{H} \boldsymbol{i} \cdot \boldsymbol{V} + D_\mathrm{bt}, \tag{26}$$

where $\boldsymbol{i}$ is the unit vector in the x direction,

$$K_\mathrm{bt} = \frac{1}{2H} \rho_0 |\boldsymbol{V}|^2 \tag{27}$$

is the kinetic energy associated with the barotropic motion, which we hereafter call barotropic kinetic energy,

$$\{\Phi, K_\mathrm{bt}\} = -\frac{1}{H} \boldsymbol{V} \cdot \nabla \Phi = -\frac{1}{H} \nabla \cdot (\Phi \boldsymbol{V}) \tag{28}$$

now denotes the rate of conversion from Φ to K_bt, and the dissipation term turns into

$$D_{\mathrm{bt}} = -\frac{K}{H}\rho_0 \boldsymbol{v}_2 \cdot \boldsymbol{V}. \tag{29}$$

We note that by subtracting (26) from (17) we could derive a complementary equation for the baroclinic kinetic energy formally defined by

$$K_{\mathrm{bc}} \equiv K - K_{\mathrm{bt}} = \frac{1}{2}\rho_0 |\boldsymbol{v}_1 - \boldsymbol{v}_2|^2 h_{\mathrm{e}},\ h_{\mathrm{e}} = \frac{h_1 h_2}{H}. \tag{30}$$

Averaging (26) over the basin yields

$$0 = \langle \Phi,\ K_{\mathrm{bt}} \rangle + \left\langle \frac{\tau^x}{H} \boldsymbol{i} \cdot \boldsymbol{V} \right\rangle + \langle D_{\mathrm{bt}} \rangle. \tag{31}$$

From this formula the difference between the cases with and without topography becomes obvious, because $\langle \Phi,\ K_{\mathrm{bt}} \rangle = 0$ when the bottom is flat everywhere. A nontrivial barotropic motion is possible in the presence of varying topography due to nonzero $\langle \Phi,\ K_{\mathrm{bt}} \rangle$. In this sense, the global quantity $\langle \Phi,\ K_{\mathrm{bt}} \rangle$ may be regarded as an energetic representation of JEBAR.

Energy diagrams corresponding to Figure 5a are shown in Figure 8 and those corresponding to Figure 5b are shown in Figure 9. Comparing the numerical values at the top and the middle of each column, we confirm that the conversion rate $\langle \Phi,\ K_{\mathrm{bt}} \rangle$ is accelerated in the presence of the bottom slopes and changes its sign seasonally so that the barotropic kinetic energy K_{bt} is substantially reduced in winter and raised above zero in summer. The other conversion rate $\langle \Phi,\ K \rangle$ is also accelerated by the bottom topography, but it has a large value even in the nontopographic case, indicating that the summer circulation in the flat-bottom ocean is supported by the baroclinic energy transfer. The value at the bottom of each column shows the result when the seasonal heat flux is included. The seasonal variation of the available potential energy $\langle \Phi \rangle$ is amplified by this thermal forcing as easily expected. It is clearly seen that the seasonal variation of the conversion rate $\langle \Phi,\ K_{\mathrm{bt}} \rangle$ is also amplified, resulting in a further reduction in the seasonal range of K_{bt}. We note that the maximum heat loss occurs in October in Exp. B1 and in December in Exp. B2 and amounts to 29 mW m^{-2} and 34 mW m^{-2}, respectively. On the other hand, the observed annual mean heat loss in the Kuroshio region is estimated to be more than 80 W m^{-2} in Oberhuber's climatology (Tomczak and Godfrey, 1994), and comparable values are obtained by recent measurements (e.g. Otobe *et al.,* 2003). Therefore, seasonal heat anomalies applied to the whole basin in the present experiments are a tiny fraction of the observed annual mean values and hence are not unrealistic.

We are now in a position to claim that bottom topography tends to stimulate energy conversion so that the transferred energy partly compensates for changes in energy storage due to both mechanical and thermal forcing. Specifically, in winter, when $\langle \Phi \rangle$ is removed

(a) winter

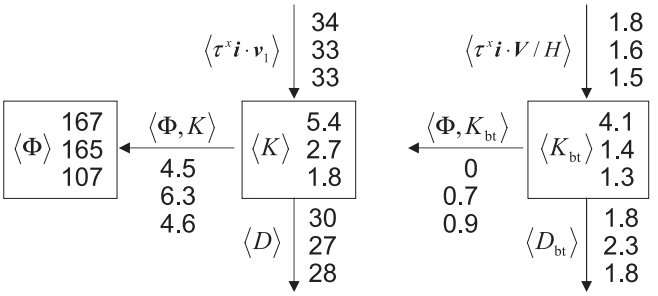

(b) summer

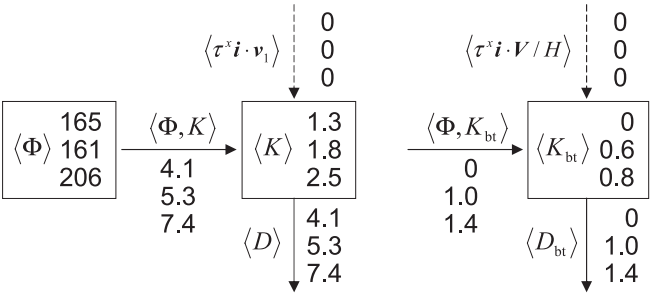

Figure 8. Basin-averaged energy diagrams in January and July, corresponding to the three cases shown in Figure 5a. The three numbers in each column correspond to (top) Exp. F1, (middle) Exp. A1 and (bottom) Exp. B1. The generation, conversion and dissipation rates are in units of mW m^{-2} and the energy storages are in units of kJ m^{-2}. The value for the state at rest is subtracted from the potential energy.

by cooling and $\langle K_{bt} \rangle$ is supplied by wind action, conversion from $\langle K_{bt} \rangle$ to $\langle \Phi \rangle$ is accelerated, while conversion in the opposite direction is accelerated in summer. This global energetic property will reflect the local behavior of the western boundary current because barotropic kinetic energy so produced propagates rapidly (instantaneously in the planetary geostrophic model) in the form of barotropic Rossby waves (Sakamoto and Yamagata, 1997). As demonstrated by the present numerical results, the summer transport may become larger than the winter transport if we take into account sufficiently intense thermal impacts from the atmosphere. We note that there is observational evidence that minimum transport events, although they have an interannual period, were accompanied with increased cooling (Lee *et al.,* 2001). In this respect, we should also investigate the effect of localized thermodynamic effects including geothermal heating described by Stommel (1982).

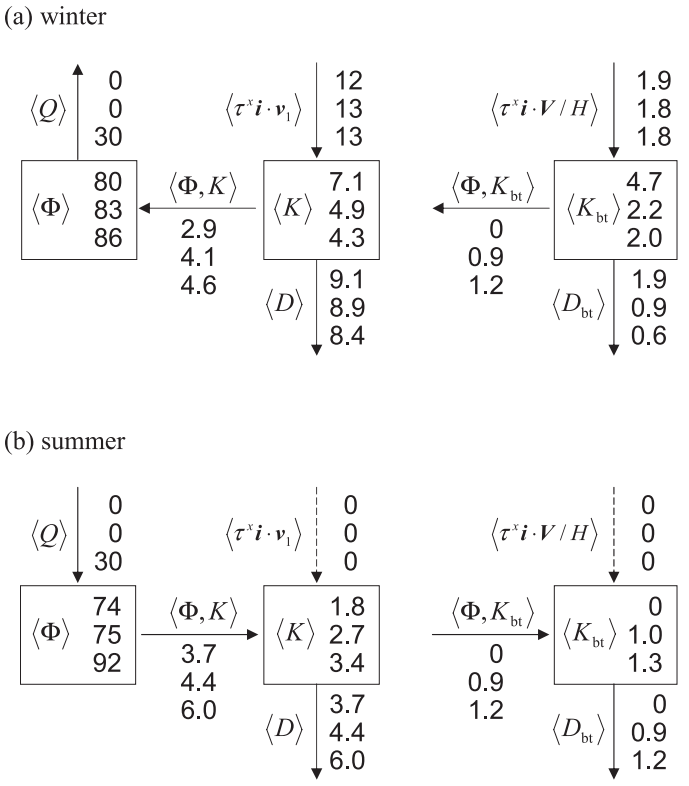

Figure 9. The same as Figure 8 but corresponding to the three cases shown in Figure 5b. The three numbers in each column correspond to (top) Exp. F3, (middle) Exp. A4 and (bottom) Exp. B2.

6. Conclusions

The observed seasonal cycle of the Kuroshio transport is characterized by an annual range of 10 Sv or less and a maximum in summer, contrary to our expectation from the nontopographic Sverdrup relation. Although some high-resolution OGCMs reproduced these key features, we have not yet explained the reason why the observations show the largest transport in summer when the subtropics are usually calm. We thus revisit this issue by conducting further numerical experiments using the same two-layer planetary geostrophic model as used by Sakamoto and Yamagata (1996) who explained the reduction of the annual range based on the JEBAR concept but did not answer the phase reversal in the transport cycle.

The findings in the present study are as follows. First, the seasonal transport variation is more sensitive to the mean thickness of the upper layer, H_1, than to the heights of the continental slope and the meridional ridge. With fixed bottom topography, the winter transport in the numerical model is rapidly reduced with decreasing H_1, whereas the summer transport is not greatly influenced. This is probably because phase speeds of

baroclinic long Rossby waves decrease with decreasing H_1, so that the baroclinic adjustment becomes less important for smaller H_1. The latter helps interactions between the water column and bottom topography which are dominant in winter but does not affect the baroclinic processes much which are dominant in summer. As a result, the annual range of the transport variation is more reduced than that in previous calculations made by some researchers using similar simple models. However, the reduction of the annual range ceases when outcropping occurs and a further decrease of H_1 merely decreases the annual mean transport. The reversal of the winter and summer transports is not realized by solely changing H_1 in the present experiments.

Secondly, the observed 180° out-of-phase relation may be reproduced by including seasonally varying heat exchange between the atmosphere and the upper ocean. In the present study this thermal forcing is represented by changing the reduced gravity with an annual period so that the negative (positive) heat transfer into the ocean decreases (increases) the available potential energy of our two-layer fluid in winter (summer). From energy budget analysis it follows that the sloping bottom enhances conversion between available potential energy and barotropic kinetic energy so that the converted energy may contribute to relaxing the impacts from the atmosphere, reminiscent of the law of mass action in chemical reactions. More specifically, winter cooling tends to accelerate the rate of conversion from kinetic to available potential energy, and vice versa in summer. Our numerical results demonstrate that if we allow for a sufficient amount of heat transfer, the relation between the winter and the summer transports can be reversed.

We conclude that the observed seasonal cycle of the Kuroshio transport may be explained within the framework of planetary geostrophic dynamics. Of course, we do not exclude the possibility of the amplification of the seasonal transport cycle by phase locking and other nonlinear processes. The global properties derived from the present energy budget analysis are experimental facts, so that in future study we should explain detailed dynamic and physical processes responsible for the seasonal changes in energy conversion.

Acknowledgments. The author wishes to thank one anonymous referee for the suggestions which significantly improved an earlier version of this paper and the other referee for a stimulating critique.

REFERENCES

Blaha, J. and R. Reed. 1982. Fluctuations of sea level in the western North Pacific and inferred flow of the Kuroshio. J. Phys. Oceanogr., *12,* 669–678.

Bogue, N. M., R. X. Huang and K. Bryan. 1986. Verification experiments with an isopycnal coordinate ocean model. J. Phys. Oceanogr., *16,* 985–990.

Chassignet, E. P. and R. Bleck. 1993. The influence of layer outcropping on the separation of boundary currents: Part I: The wind-driven experiments. J. Phys. Oceanogr., *23,* 1485–1507.

Cloke, P. and M. J. P. Cullen. 1994. A semi-geostrophic ocean model with outcropping. Dyn. Atmos. Oceans, *21,* 23–48.

Haltiner, G. J. and R. T. Williams. 1980. Numerical Prediction and Dynamic Meteorology, 2nd ed., John Wiley & Sons, NY, 477 pp.

Hellerman, S. and M. Rosenstein. 1983. Normal monthly wind stress over the world ocean with error estimates. J. Phys. Oceangr., *13,* 1093–1104.

Holton, J. R. 1992. An Introduction to Dynamic Meteorology, 3rd ed., Academic Press, San Diego, Tokyo, 511 pp.

Huang, R. X. 1991. The three-dimensional structure of wind-driven gyres: Ventilation and subduction. Rev. Geophys. Suppl; 590–609.

Ichikawa, H. and R. C. Beardsley. 1993. Temporal and spatial variability of volume transport of the Kuroshio in the East China Sea. Deep-Sea Res. I, *40,* 583–605.

Ichikawa, H. and M. Chaen. 2000. Seasonal variation of heat and freshwater transports by the Kuroshio in the East China Sea. J. Mar. Sys., *24,* 119–129.

Isobe, A. and S. Imawaki. 2002. Annual variation of the Kuroshio transport in a two-layer numerical model with a ridge. J. Phys. Oceanogr., *32,* 994–1009.

Kagimoto, T. and T. Yamagata. 1997. Seasonal transport variations of the Kuroshio: An OGCM simulation. J. Phys. Oceanogr., *27,* 403–418.

Kawabe, M. 1988. Variability of Kuroshio velocity assessed from the sea-level difference between Naze and Nishinoomote. J. Oceanogr. Soc. Japan, *44,* 293–304.

Lee, T. N., W. E. Johns, C.-T. Liu, D. Zhang, R. Zantopp and Y. Yang. 2001. Mean transport and seasonal cycle of the Kuroshio east of Taiwan with comparison to the Florida Current. J. Geophys. Res., *106,* 22143–22158.

Mertz, G. and D. G. Wright. 1992. Interpretations of the JEBAR term. J. Phys. Oceanogr., *22,* 301–305.

Minami, H., E. Kamihira, K. Komura, H. Eguchi and J. Nishizawa. 1978. Statistical features of the oceanographic conditions south of Honshu, Japan. Part 1. Summer and winter off Kii Peninsula (in Japanese with English abstract). Umi To Sora, *53,* 147–156.

——1979. Statistical features of the oceanographic conditions south of Honshu, Japan. Part 2. In spring and autumn off Kii Peninsula (in Japanese with English abstract). Bull. Kobe Mar. Obs., *197,* 1–11.

Niiler, P. P. and W. S. Richardson. 1973. Seasonal variability of the Florida Current. J. Mar. Res., *31,* 144–167.

Otobe, H., K. Taira, S. Kitagawa, T. Asai and K. Hanawa. 2003. Variability of upper ocean heat balance in the Shikoku Basin during the ocean mixed layer experiment (OMLET). J. Oceanogr., *59,* 619–627.

Parsons, A. T. 1969. A two-layer model of Gulf Stream separation. J. Fluid Mech., *39,* 511–528.

Qiu, B. 1992. Recirculation and seasonal change of the Kuroshio from altimetry observations. J. Geophys. Res., *97,* 17801–17811.

Qiu, B. and T. M. Joyce. 1992. Interannual variability in the mid- and low-latitude western North Pacific. J. Phys. Oceanogr., *22,* 1062–1079.

Sakamoto, T. 1999. On discontinuities in the Sverdrup interior. J. Phys. Oceanogr., *29,* 2457–2461.

——2003. On the structure of the wind-driven circulation in two-layer models, *in* Recent Research Developments in Physical Oceanography, *2,* Transworld Research Network, Trivandrum, 1–43.

Sakamoto, T. and T. Yamagata. 1996. Seasonal transport variations of the wind-driven ocean circulation in a two-layer planetary geostrophic model with a continental slope. J. Mar. Res., *54,* 261–284.

——1997. Evolution of baroclinic planetary eddies over localized bottom topography in terms of JEBAR. Geophys. Astrophys. Fluid Dyn., *84,* 1–27.

Salmon, R. 2002. Numerical solution of the two-layer shallow water equations with bottom topography. J. Mar. Res., *60,* 605–638.

Schott, F. A., T. N. Lee and R. Zantopp. 1988. Variability of structure and transport of the Florida Current in the period range of days to seasonal. J. Phys. Oceanogr., *18,* 1209–1230.

Stommel, H. 1982. Is the South Pacific helium-3 plume dynamically active? Earth Planet. Sci. Lett., *61,* 63–67.

Stommel, H. and G. Veronis. 1980. Barotropic response to cooling. J. Geophys. Res., *85,* 6661–6666.

Taft, B. 1972. Characteristics of the flow of the Kuroshio south of Japan, *in* Kuroshio, Its Physical Aspects, H. Stommel and K. Yoshida, eds., Univ. of Tokyo Press, Tokyo, 517 pp.

Tomczak, M. and J. S. Godfrey. 1994. Regional Oceanography: An Introduction, Pergamon, Oxford, England; New York, 422 pp.

Toro, E. F. 1997. Riemann Solvers and Numerical Methods for Fluid Dynamics: A Practical Introduction, Springer, Berlin, Heidelberg, 592 pp.

Welander, P. 1966. A two-layer frictional model of wind-driven motion in a rectangular oceanic basin. Tellus, *18,* 54–62.

Yee, H. C. 1987. Construction of explicit and implicit symmetric TVD schemes and their applications. J. Comput. Phys., *68,* 151–179.

Zhang, D., W. E. Johns and T. N. Lee. 2002. The seasonal cycle of meridional heat transport at 24°N in the North Pacific and in the global ocean. J. Geophys. Res., *107*(C7), 3083, 10.1029/2001JC001011.

Received: *18 June, 2004;* revised: *27 January, 2005.*